CHEMISTRY OF MATERIALS

pubs.acs.org/cm

Article

Synthesis of Edge-Shared Octahedral $MAPbBr_3$ via Pressure- and Temperature-Induced Multiple-Stage Processes

Mei Li, Kejun Bu, Junlong Li, Hao Wang, Yixuan Xu, Songhao Guo, Hui Luo, Bingyan Liu, Dongliang Yang, Yu Gong, Yonggang Wang, Yufeng Liu, Xujie Lü,* and Chuanlong Lin*

Cite This: https://doi.org/10.1021/acs.chemmater.2c03172

Read Online

HPSTAR 1620-2023

ACCESS | Metrics & More | Article Recommendations | Supporting Information

ABSTRACT: Organic–inorganic halide perovskites possess flexible structures with tunable optical properties at high pressures, but the pressure-induced amorphization limits the understanding and exploration of the structure–property relationships. Herein, we report an edge-shared octahedral $MAPbBr_3$ via multiple-stage transformation of the traditional corner-shared three-dimensional perovskites at high-pressure and high-temperature ($P-T$) conditions. In situ synchrotron X-ray diffraction reveals that upon heating at 8.7 GPa, the amorphized $MAPbBr_3$ transforms into a high $P-T$ structure above 654 K via multiple-stage crystallization. The high $P-T$ phase is determined to be a monoclinic $P2/m$ structure with layered edge-shared Pb–Br octahedra, which can be quenched to RT at high pressures but converts back to the initial cubic perovskite structure below 0.7 GPa under decompression. The Raman and optical measurements demonstrate that the high $P-T$ phase has similar vibrational behavior and tunable optical properties to those of the pressure-induced amorphous phase, indicating the similarity in the local structure with the edge-shared $PbBr_6$ octahedral frame and the MA organic cations between the high $P-T$ phase and the amorphous state. The present results demonstrate the structural diversity and interconversion in $MAPbBr_3$ by overcoming the large kinetic barrier derived from the anisotropic organic cations and disordering arrangement of the Pb–Br octahedra, providing new insights into the understanding of structural transitions and amorphization of halide perovskites.

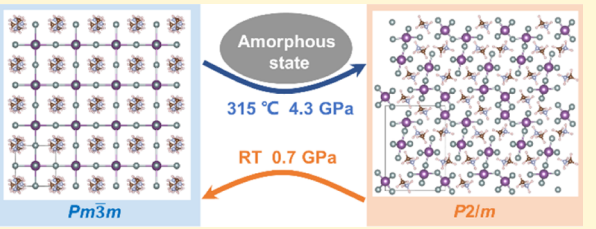

1. INTRODUCTION

Metal halide perovskites (MHPs) and perovskite-related materials exhibit exceptional optoelectronic properties, which are promising for applications in solar cells,[1,2] light-emitting diodes,[3,4] and photodetectors.[5] The three-dimensional (3D) MHPs with a general chemical formula of ABX_3, where A = $CH_3NH_3^+$ (MA), $CH(NH_2)_2^+$ (FA), or Cs^+; B = Pb^{2+}, Sn^{2+}, or Ge^{2+}; X = Cl^-, Br^-, or I^-, are constructed by corner shared octahedra and each A-site cations sits in the cavity formed by eight octahedra. The inorganic metal halide octahedral building blocks dominate the unique properties of MHPs and their complex relationship with A-site cations provides additional tunability of the crystal structures. Beyond the 3D compounds, the MHP analogues with edge- or face-shared octahedra are also of considerable interest owing to the higher stability and structural diversity. The structural diversity of MHPs and the interconversion between perovskites and analogues can be realized with chemical tailoring such as the exchange of cations or anions within the lattice,[6−8] vacancy control,[9,10] and dimensional manipulations.[8,11] However, the tunability of the structures and properties is limited by the ionic radius with the criterion of tolerance factor.[12] Pressure provides an alternative method to effectively modulate the crystal lattices and electronic configurations of MHPs by altering the interatomic distances and electronic orbitals but without changing the chemical compositions.[13]

In the last few decades, increasing numbers of research on MHPs under high pressure have been reported,[14−21] adding numerous new structures with novel physical properties to the family of perovskite materials. In inorganic MHPs, for instance, $CsPbI_3$ and $CsPbBr_3$ have been reported to undergo the conversion from the $Pm\bar{3}m$ perovskite structure with corner-shared BX_6 octahedra to the $Pnma$ structure with double chains of edge-shared PbX_6 under pressure;[22,23] 2D $CsPb_2X_5$ (X = Br and I) with face-shared BX_6 octahedra (space group $I4/mcm$) was synthesized by the direct phase separation of 1D $CsPbI_3$ with edge-shared PbX_6 octahedra (space group $C2/m$) at high-pressure and temperature ($P-T$) conditions.[24] The tunable connectivity modes of BX_6 octahedra observed in inorganic MHPs under high $P-T$ conditions provide a new possibility for the design and synthesis of more perovskite-related structures, but the underlying mechanisms remain

Received: October 17, 2022
Revised: January 14, 2023

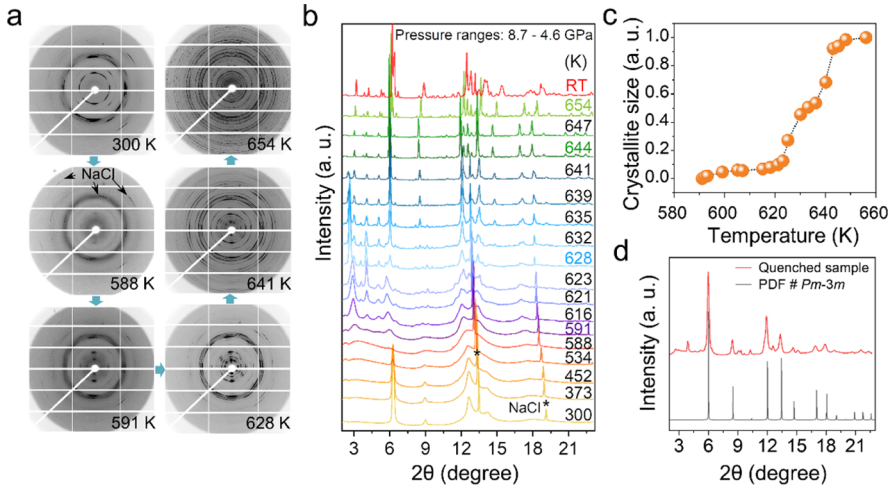

Figure 1. In situ structural characterization of $MAPbBr_3$ under high $P-T$ conditions. (a) Two-dimensional raw XRD images at six selected temperature points and (b) one-dimensional integrated XRD profiles. NaCl was used as the pressure calibrant. (c) Normalized grain size as a function of temperature during the crystallization process. (d) Integrated XRD patterns of the sample quenched under ambient conditions in comparison with the PDF card of original cubic perovskite $MAPbBr_3$ with the space group of $Pm\bar{3}m$.[18]

unclear in organic MHPs due to the limitation of the pressure-induced amorphization and temperature-induced decomposition. In this work, we control the thermodynamic parameters of both pressure and temperature and select $MAPbBr_3$ as an example to explore the new structures and physical properties.

As a typical 3D MHPs, $MAPbBr_3$ adopts cubic perovskite structures with a $Pm\bar{3}m$ symmetry at ambient conditions and converts to a cubic $Im\bar{3}$ structure at ~0.4 GPa, followed by the transformation into an orthorhombic perovskite phase with the *Pnma* space group at 1.8 GPa.[18,25−27] Meanwhile, the band gap of $MAPbBr_3$ exhibits a V-shape change, namely, a red shift from ambient pressure to 0.9 GPa and then blue-shifts.[25,28,29] Upon further compression from 2 to 34.0 GPa, a reversible amorphization occurs, accompanied by the decreasing of the band gap.[25] Different from the isotropic metal ions (such as Cs^+) in the A-site of the inorganic MHPs, the pressure-induced amorphization in the organic MHPs may be derived from the directionality of MA and distortion of the $PbBr_6$ octahedron, leading to the large kinetic barrier in the pressure-induced phase transformation of the corner-shared octahedral perovskite into the thermally denser crystalline phases.[25,30] This restricts the exploration of the structural interconversion between the crystalline phases with different connectivity modes of the octahedra and also limits the understanding of the structure−property relationship of organic MHPs. In this work, we demonstrated two transition routes for the formation of an edge-shared octahedral $MAPbBr_3$ via multiple-stage transformation of the cornered-shared octahedral perovskites at high $P-T$ conditions. The multiple-stage crystallization of the amorphized $MAPbBr_3$ is uncovered, which is distinguished from inorganic MHPs with isotropic metal ions in the A-site, in the formation of a high-pressure crystalline phase.

2. EXPERIMENTAL SECTION

2.1. Sample Preparation. $MAPbBr_3$ (CH_3NH_3PbBr) perovskite crystals were prepared from a solution using a previously reported method.[25,31,32] Methylammonium halide precursors CH_3NH_3Br were synthesized through the reaction of hydrobromic acid HBr with methylamine followed by recrystallization from ethanol. An equimolar amount of HBr acid solution in water was added dropwise into methylamine (40% in methanol) in an ice bath and stirred for 2 h. Removal of the solvent was followed by recrystallization from ethanol to yield CH_3NH_3Br crystals. A total of 0.23 g freshly prepared CH_3NH_3Br and 0.72 g $PbBr_2$ were mixed in 4 mL *N*-dimethylformamide (~40 wt %) at 60 °C and stirred for 12 h. Then, the precursor solution was heated at 65 °C under the vacuum for 24 h to produce orange $CH_3NH_3PbBr_3$ crystals.

2.2. Generation of High $P-T$ Conditions. The high-pressure environment was provided by symmetric diamond anvil cells (DACs) with 400 μm anvil culets. Stainless-steel (T301) gaskets were pre-indented to 30−40 μm in thickness and holes of about 150 μm diameter were laser-drilled to serve as the sample chambers. No pressure-transmitting medium was used. The $MAPbBr_3$ and a ruby ball and/or NaCl were loaded together into the sample chamber. The pressure calibration was determined utilizing the ruby fluorescence method.[33] The generation of high $P-T$ conditions is similar to that previously reported in $CsPbI_3$.[24]

2.3. High $P-T$ X-ray Diffraction Measurements. In situ synchrotron high $P-T$ X-ray diffraction (XRD) experiments were conducted at the beamline 4W2, Beijing Synchrotron Radiation Facility (BSRF) with a wavelength of 0.6199 Å. The X-ray beam was focused in the horizontal and vertical direction to a 16 μm × 8 μm (full width at half-maximum) spot using Kirkpatrick-Baez mirrors, and CeO_2 was used as the standard sample for calibration. XRD patterns were collected with a Pilatus 3 2 M detector. The image of patterns is obtained at 10−50 °C intervals and each image was collected for 100 s. In situ high-pressure XRD experiments for the investigation on the structure of original $MAPbBr_3$ were conducted with an average acquisition time of 50 s at RT. The diffraction patterns were integrated into a one-dimensional profile by using the Dioptas software.[34] Structure refinements were carried out using the Le bail method, using General Structure Analysis software (GSAS).[35]

2.4. In situ High-Pressure Vibrational and Optical Measurements. The high-pressure environment was provided by symmetrical DACs. Type II-a ultralow fluorescence diamonds with 400 μm anvil culets were used. Raman experiments were carried out on a Renishaw micro-Raman spectroscopy system equipped with a second-harmonic Nd:YAG laser (operating at 633 nm) in a backscattering geometry for excitation and signal collection. The system was calibrated by the Raman peak of the standard Si sample. In situ high-pressure UV−vis absorption spectra, photoluminescence (PL) spectra, optical images, and fluorescence images were collected in a home-designed spectroscope system in a micro-region (Gora-UVN-FL, built by Ideaoptics, Shanghai, China). The absorption spectra were measured using a Xenon light source between 200 and 1700 nm. The PL spectra were measured using a 405 nm laser excitation at a power of 10 mW.

https://doi.org/10.1021/acs.chemmater.2c03172
Chem. Mater. XXXX, XXX, XXX−XXX

3. RESULTS AND DISCUSSION

3.1. Multiple-Stage Transformations from Perovskite to High-Pressure Crystalline $MAPbBr_3$. The cubic perovskite $MAPbBr_3$ was loaded in DACs for high-pressure studies. Upon compression at room temperature (RT), the perovskite $MAPbBr_3$ underwent two pressure-induced crystal−crystal transitions below 2 GPa (from $Pm\bar{3}m$ to $Im\bar{3}$ and then to $Pnma$) (Figure S1). When the pressure increases to over 3.2 GPa, the structural disordering occurred with Bragg diffraction peak broadening and disappearing. Above 8 GPa, the broadbands of the amorphous state were dominated with a few peaks remaining in the XRD profiles. The pressure-induced transition sequence of $MAPbBr_3$ at RT was consistent with the previous report[25] and the amorphous state observed was considered as an intermediate state due to the insufficient thermal energy to overcome the kinetic barrier in the transformation of perovskite $MAPbBr_3$ into the high-pressure crystalline phase.[36−39] This leads to the question regarding what is the high-pressure crystalline phase.

To explore the high-pressure crystalline phase, we heated the amorphous $MAPbBr_3$ in an externally heated DAC at 8.7 GPa. The structural evolution in the crystallization process of the amorphous $MAPbBr_3$ was monitored by in situ XRD. Figure 1 shows that the crystal Bragg diffraction peaks of the original perovskite $MAPbBr_3$ disappeared gradually upon heating with pure broad diffuse reflection appearing at 588 K, indicating completely structural amorphization (Figure 1a,b). Upon further heating, the amorphous $MAPbBr_3$ started to crystallize with several broad crystal diffraction peaks appearing at 591 K. Above 628 K, the broad crystal peaks became sharp and split, accompanied by new diffraction reflections emerging. For instance, the diffraction peak at 2.88° split into a strong peak at 2.65° and a weak peak at 3.01°. Upon heating the sample up to 641 K, another phase transition occurred, which was evidenced by the disappearance of the old diffraction peaks at 2.51° and the appearance of new peaks at 3.78°, as well as the obvious splittings of diffraction peaks at 5.10 and 6.05° (Figure S2). Under further heating from 644 to 654 K, neither peaks disappeared nor new peaks appeared with only crystal diffraction peak sharpening. This implies the formation of a stable high $P-T$ phase of $MAPbBr_3$ above 644 K. The transition sequence observed above demonstrated multiple-stage kinetic processes from the perovskite structure to the stable denser crystalline $MAPbBr_3$ under high $P-T$ conditions.

The crystal grain size in the crystallization of the amorphous sample during the heating process was estimated using the Debey−Scherrer equation with $D = K\lambda/(\beta \cos \theta)$, where K is a dimensionless shape factor, λ is the X-ray wavelength, β is the full width at half maximum (FWHM) of the diffraction peak, θ is the Bragg angle, and D is the average crystallite size. The FWHM of the diffraction profile was contributed by the instrumental broadening and the grain size. Here, the calculated grain size, normalized by the value at 644 K, is used to reflect the trend of the crystal growth with temperature. As shown in Figure 1c, three stages are presented in the crystallite size as a function of temperature. The crystallinity during the crystallization process increased slowly in the grain size from 591 to 623 K, then grew sharply up to 644 K, and finally reached a plateau above 644 K. This corresponded to the multiple-stage kinetic processes in the phase transformation into the stable crystalline $MAPbBr_3$.

The structural evolution of $MAPbBr_3$ under high $P-T$ conditions is repeatable. It is found that both the high $P-T$ phase and the intermediate metastable phases obtained in the crystallization processes can be quenched to ambient temperature at high pressure (Figures 1b and S3 and S4). In the present work, we focus on the final high $P-T$ crystalline phase. Under decompression of the high $P-T$ phase, the crystal diffraction peaks shifted to a low angle. Below 0.7 GPa, the high $P-T$ phase transformed back into the cubic perovskite phase with some residual peaks of the high $P-T$ phase at ambient pressure (Figures 1d and S4). Notably, the diffraction peaks of the recovered sample at ambient conditions were broad and weak with the coexistence of perovskites and high $P-T$ phases. When the recovered sample was heated above 365 K, the high $P-T$ phase transformed completely into the cubic perovskite structure, implying that thermal energy was required for the phase transformation of the high $P-T$ phase back into perovskite $MAPbBr_3$ (Figure S5). This also means the high $P-T$ phase of $MAPbBr_3$ may be retained at ambient pressure at low temperatures (such as at liquid nitrogen temperature). When compressing the perovskite $MAPbBr_3$ up to 3.7 GPa at high temperatures; interestingly, the perovskite phase transformed directly into the intermediate crystalline phase without amorphization, which is associated with the new crystal diffraction peaks emerging and the parent peaks disappearing. The formation of high $P-T$ phases can be repeated via the heating−compression path, as well as the compression−heating path, implying the amorphous $MAPbBr_3$ served as an intermediate state at high pressures (Figure S6). It should be noted that the conversion of the high $P-T$ phase back to the perovskite $MAPbBr_3$ at RT implied no decomposition of $MAPbBr_3$ into MABr and $PbBr_2$ at high $P-T$ conditions.

3.2. Crystal Structure of the Stable High $P-T$ Crystalline Phase. The low diffraction angles with large d-spacing values and lots of diffraction peaks implied the low symmetry of the structure for the high $P-T$ phase, making it difficult to determine the crystal structure accurately via the powder diffraction data. The high $P-T$ phase cannot be attributed to the structure with corner-shared octahedra in indexation, which is limited by the extinction examination. It is also not the decomposed products ($PbBr_2$ and MABr) of $MAPbBr_3$, as the high $P-T$ phase can transform back directly into the cubic perovskite under decompression at room (or high) temperature. If so, the chemical reaction should occur in the products at a high temperature.[40] Thus, it is reasonable to speculate the high $P-T$ crystalline $MAPbBr_3$ may have an edge-shared octahedral structure, such as the structural transition from the corner-shared octahedra to the edge-shared octahedral structure in $CaRhO_3$.[41] However, distinguished from $CaRhO_3$ with space group $P2_1/m$, the A-site ions in an organic halide perovskite have directionality and intramolecular interactions, which may result in a crystal structure with a lower symmetry for the high $P-T$ phase. To confirm the speculation, the structure of the high $P-T$ phase is analyzed based on the XRD data.

Using the program Dicvol, all diffraction peaks of the high $P-T$ crystal structure of $MAPbBr_3$ can be well indexed into a monoclinic phase and the space group is determined tentatively to be $P2/m$ according to the reflection conditions. The monoclinic structure of the high $P-T$ phase with a quasi-2D structure may be obtained by expanding three times along the b axis of the $CaRhO_3$. Referring to the structure of

https://doi.org/10.1021/acs.chemmater.2c03172
Chem. Mater. XXXX, XXX, XXX−XXX

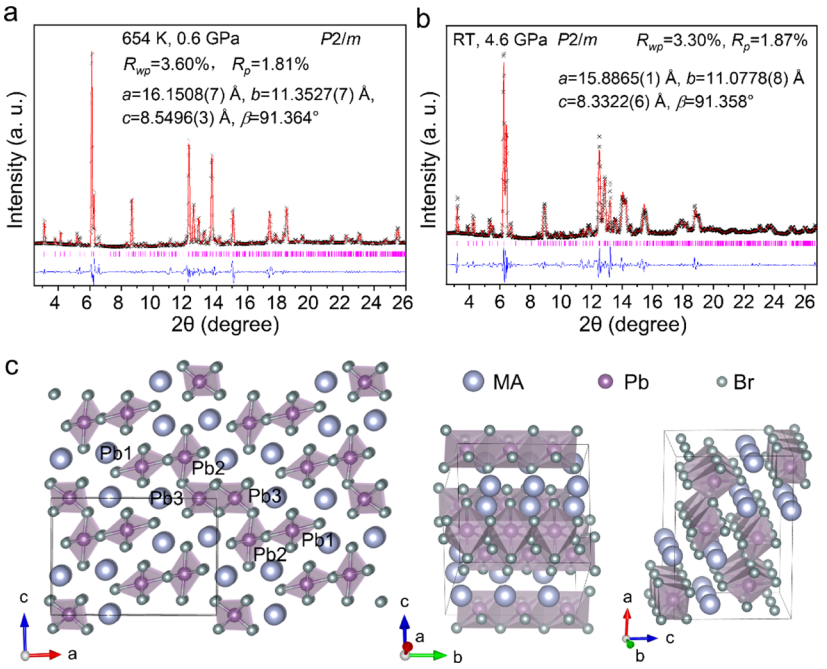

Figure 2. Full profile refinement for the high $P-T$ phase of $MAPbBr_3$. (a) at 654 K and (b) quenched to RT. Symbols: observed patterns; red solid line: calculated patterns; plum vertical line: diffraction positions of the monoclinic phase; blue solid line: differences between the observed and calculated patterns. (c) Schematic diagrams of the crystal structure of the high $P-T$ phase referring to $CaRhO_3$.[41]

$CaRhO_3$, a full profile refinement for the high $P-T$ phase of $MAPbBr_3$ yielded a good enough resolution for a peak assignment (Figure 2). The unit cell parameters of the high $P-T$ phase were a = 16.1508(7) Å, b = 11.3527(7) Å, c = 8.5396(3) Å, β = 91.364°, and V = 1565.3(1) Å^3 at 654 K (Figure 2a) and a = 15.8865(1) Å, b = 11.0778(8) Å, c = 8.3322(6) Å, β = 91.358°, and V = 1465.9(1) Å^3 at RT (Figure 2b). The volume was 12% denser at 4.6 GPa than the corner-shared octahedral perovskite. The crystal structure of the high $P-T$ phase is illustrated in Figure 2c. Each $PbBr_6$ octahedron shared the edges with the nearest neighbor $PbBr_6$ octahedra to form single $PbBr_6$ octahedral chains parallel to the b-axis. Pb_1Br_6 octahedral chains and Pb_2Br_6 octahedral chains shared the corners of octahedra to form chains. Two Pb_3Br_6 octahedral chains shared edges to form a double chain, similar to that in δ-$CsPbI_3$. Similar structures with both edge- and corner-shared octahedra have been reported in 2D halide perovskites,[42,43] where the configurational strain imposed by the organic cations to the inorganic skeleton breaks the standard connectivity mode of $PbBr_6$ octahedra and instead stabilizes an edge-shared network. It should be noted that this is a probable structure and the precise crystal structure may need to be confirmed in further studies.

3.3. Vibrational and Optical Properties of the High $P-T$ Phase. To explore the structural feature of both organic MA and inorganic octahedral blocks and understand the relationship between the high $P-T$ phase and the original perovskite phase of $MAPbBr_3$, vibrational and optical properties were investigated by using high-pressure Raman spectroscopy and absorption spectra at RT. In Raman spectra, the low-frequency vibrational modes (ν_1 and ν_2) with broad features at 50−250 cm^{-1} were assigned to the lattice vibration of the Pb−Br octahedral frame (Figure 3a); in contrast, the high frequencies (ν_3−ν_5) at 300−3200 cm^{-1} were assigned to vibrational modes of the MA organic cations (Figures 3b,c and S8), which was affected by the distortion and tilting of $PbBr_6$ octahedra around MA.[32,44,45] In situ high-pressure Raman of the original perovskite phase of $MAPbBr_3$ and the detailed analysis can be seen in Figure S7, Supporting Information. Briefly, the vibrational modes of the initial perovskite $MAPbBr_3$ underwent distinct changes for the vibration of MA and octahedra block in the amorphization above 4.5 GPa, which was associated with a structural phase transition in the previous report.[46] The phase transition derives from the serious distortion and tilting of the adjacent octahedron and orientationally disordered MA under compression.[30,47,48] Interestingly, the vibrational modes of the high $P-T$ phase of $MAPbBr_3$ is similar to that of the amorphous phase. This implies the high $P-T$ phase has a local structure in both edge-

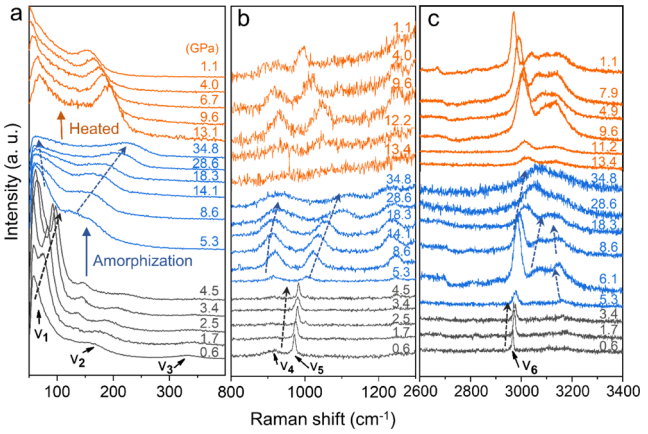

Figure 3. Selected Raman spectra of $MAPbBr_3$ within (a) 50−400, (b) 800−1300, and (c) 2600−3400 cm^{-1}. The color shows different phases of $MAPbBr_3$ with elevated pressure, that is, the original crystal phase (black), the amorphous phase (blue), and the high $P-T$ phase quenched to RT (orange). An excitation wavelength of 632 nm is used to avoid the fluorescence background.

https://doi.org/10.1021/acs.chemmater.2c03172
Chem. Mater. XXXX, XXX, XXX−XXX

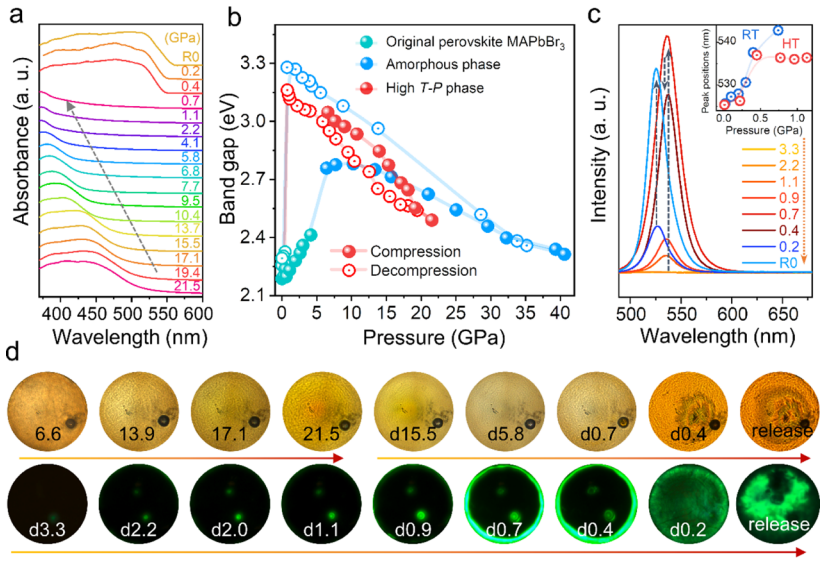

Figure 4. Pressure-dependent optical properties of high $P-T$ phase. (a) UV−vis absorption during decompression. (b) Optical band gap of the original perovskite phase (blue), amorphous phase (glaucous), and high $P-T$ phase (red) under various pressures. (c) In situ PL spectra of high $P-T$ phase during decompression. Inset: PL peak position as a function of pressure (decompression), compared with the original $MAPbBr_3$ phase, shows a fine position switch from 538 to 525 nm. (d) Optical and fluorescent images at the selected pressures. The uneven color in the sample chamber is attributed to the non-hydrostatic pressure condition.

shared $PbBr_6$ octahedral frame and the MA organic cations similar to the amorphous phase.

Optical properties of the high $P-T$ phase were studied via the UV−vis absorption and PL measurements under high pressure (Figure 4). At ambient conditions, the original perovskite $MAPbBr_3$ exhibited a sharp absorption edge near 560 nm with a corresponding optical band gap of 2.19 eV. The absorption and band gap of original $MAPbBr_3$ during compression−decompression processes are shown in Figures S9 and S10.

The absorption of the high $P-T$ phase exhibited a continuously red shift with pressure increasing (Figure S11). At 21.5 GPa, the absorption edge of the high $P-T$ phase was located at ∼500 nm with a band gap of 2.48 eV. However, the absorption of the high $P-T$ phase shown remarkable changes during decompression. As shown in Figure 4a, the absorption edge underwent a distinct blue shift to 400 nm above 0.7 GPa, corresponding to a huge increase in the band gap (Figures 4b and S11). Thereafter, it exhibited a sudden red shift to 540 nm with a band gap of 2.28 eV when the pressure was released to 0.4 GPa, attributing it to the high $P-T$ phase recovery to the original perovskite phase observed in the XRD measurements. Correspondingly, the colors of the sample changed from light yellow to dark yellow during compression (Figure 4d). Upon decompression, the sample gradually became colorless and then suddenly converted to orange below 0.4 GPa. Notably, the band gap evolution of the high $P-T$ phase is similar to that of the amorphous phase (Figures S12 and S13), which confirmed the similarity in the band structure.

The high-pressure PL spectroscopy and fluorescent images were conducted to explore the variations of emission property for the high $P-T$ phase of $MAPbBr_3$. The original perovskite phase of $MAPbBr_3$ exhibited a broadband emission located at 525 nm (Figure S14). In the high $P-T$ phase, the PL emission can be detectable below 3.3 GPa during decompression and was located at 538 nm. The PL intensity of the high $P-T$ phase shows a remarkable enhancement and reached a maximum at 0.7 GPa and then dropped under decompression from 0.7 to 0.4 GPa due to phase transformation from the high $P-T$ phase into the perovskite $MAPbBr_3$ (Figures 4c and S15). Subsequently, the peak position shows a blue shift to 526 nm at 0.2 GPa and the PL intensity raised continuously under further decompression from 0.2 GPa to ambient pressure. The inset of Figure 4c shows the PL peak position as a function of pressure, where a slight difference of emission property was observed between the high $P-T$ phase and the amorphous $MAPbBr_3$ below 1 GPa. In addition, the fluorescent micrographs in Figure 4d exhibit the PL brightness variations during the decompression process.

Theoretical calculations reported that the conduction band minimum is mainly dominated by Pb-6p orbitals, while the valence band maximum mainly consists of Br-4p orbitals.[25] This indicates the band gap of $MAPbBr_3$ is mainly governed by the $PbBr_6$ octahedra and the MA cations do not contribute to the band gap directly. Remarkably, the band gap of perovskites with corner-shared octahedra is smaller than that of the perovskite-related materials with edge-shared octahedra, which has been evidenced in the MHPs with two different connectivity modes of PbX_6 octahedra.[25,49−51] For instance, the band gap of the γ-$CsPbBr_3$ with corner-shared octahedra was ∼2.3 eV, while that of the δ-$CsPbBr_3$ with edge-shared octahedra was ∼2.9 eV;[23,52] the black α-$CsPbI_3$ with octahedra shared by the corners had a band gap of only ∼1.7 eV, but ∼2.6 eV in the yellow δ-$CsPbI_3$ with octahedra shared by the edges.[53,54] These demonstrate that the discrepancy in the band structure between the high $P-T$ phase and the initial perovskite phase arises from the disparity in the $PbBr_6$ octahedral arrangement. Besides, both Raman and PL further confirmed the distinctively local octahedral structure in the high $P-T$ phase different from the initial corner-shared perovskite phase.

3.4. Transition Mechanism in the Formation of High $P-T$ Crystalline Phase. The XRD peaks of crystalline $MAPbBr_3$ are highly related with the long-range ordered packing of heavy atoms Pb and Br, as the MA organic cations, consisting of light atoms (i.e., C, N, and H), only contribute to

https://doi.org/10.1021/acs.chemmater.2c03172
Chem. Mater. XXXX, XXX, XXX−XXX

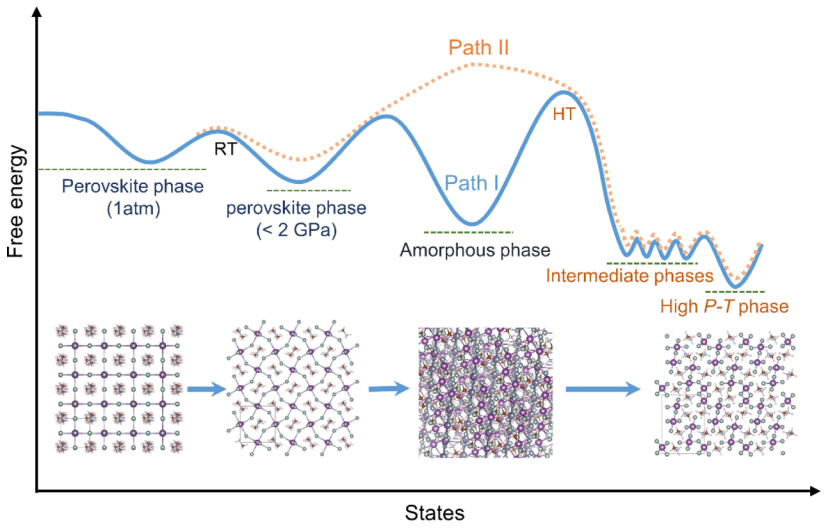

Figure 5. (a) Schematic diagram for two transition paths in the phase transformation of $MAPbBr_3$ at high $P-T$ conditions. Path I (blue line): The phase transition sequence is cubic perovskite → orthorhombic perovskite → amorphous $MAPbBr_3$ at high pressure and RT, followed by multiple-stage crystallization of amorphous $MAPbBr_3$ at high $P-T$ conditions; path II (orange dotted line): the transformation from the initial perovskite structure into a denser high $P-T$ phase without amorphization under compression at high temperatures. Bottom: the pictorial configurations of Pb−Br inorganic skeleton and the MA organic cations on increasing pressure and/or temperature.

the broad diffraction background. The vibrational and optical measurements demonstrated that the amorphous phase has a local structure in both edge-shared Pb−Br octahedral frame and the MA organic cations similar to the high $P-T$ phase. Therefore, the amorphous $MAPbBr_3$, indicated by the halo peaks in the diffraction patterns, reflects a disordered arrangement of the $PbBr_6$ octahedra. This raises questions regarding what reason causes the disordering of the octahedra in the pressure-induced amorphization. How to synthesize the high-pressure phase bypassing the amorphous state? Is the kinetic mechanism in $MAPbBr_3$ unique or ubiquitous in inorganic and organic MHPs?

At ambient conditions, $MAPbBr_3$ adopted a cubic structure with regular $PbBr_6$ octahedra and dynamically rotating MA molecules.[55−57] With increasing pressure up to 1.8 GPa, the cubic perovskite structure underwent $Pm\bar{3}m \rightarrow Im\bar{3} \rightarrow Pnma$ transitions with a lattice contraction, accompanied with frozen MA ligands and distortion of the $PbBr_6$ octahedron. The octahedron is connected with MA through the N−H···Br hydrogen bonding. Previous studies demonstrated that the anisotropy of the organic cations is a crucial factor to affect asymmetric deformation of the octahedral framework under compression,[28,30,45,58] giving rise to the distortion of the $PbBr_6$ octahedra at high pressures with deviation from the perfect local octahedral symmetry.[53,59] Upon further compression above 4.5 GPa, application of pressure leads to the atomic distance shortening and the enhanced N−H···Br interactions. The anisotropy of the MA cation causes more deformation of the octahedron. Thus, it is reasonable to speculate that the disordered arrangement and distortion of the octahedra, indicated by the X-ray diffraction, in the pressure-induced amorphization of $MAPbBr_3$ may be attributed to the strong anisotropic interactions between the orientational MA cation and inorganic octahedron.[60] Meanwhile, it will lead to a large kinetic barrier in the phase transformation from the corner-shared octahedral perovskites into the high-pressure denser crystalline phase with an edge-shared octahedron. It should be noted that the amorphization could be enhanced by deviatoric stress at the non-hydrostatic condition by promoting the deformation of the octahedra.[61,62]

Interestingly, thermal energy, provided by heating, can be applied to overcome the energy barrier and rendered into two distinctively different transition routes in the phase transformation from the corner-shared octahedral perovskite $MAPbBr_3$ into the high-pressure edge-shared octahedral crystalline phase, viz., multiple-stage crystallization of the amorphized $MAPbBr_3$ upon heating at high pressures (path I, blue line in Figure 5), and direct phase transformation of the cubic perovskite into the high-pressure crystalline phase under compression at high temperatures (path II, orange dotted line in Figure 5). In path I, the perovskite structure undergoes pressure-induced amorphization first owing to the lower kinetic barrier; then, the amorphous $MAPbBr_3$ as an intermediate state is structurally relaxed to crystallize into the edge-shared crystalline phase. It should be noted that several intermediate crystalline phases were observed in the crystallization of the amorphous $MAPbBr_3$. This demonstrates the structural diversity and potential interconversion between them. In path II, the perovskite structure can transform directly into the high-pressure crystalline phase, as the thermal energy is sufficient to overcome the large kinetic barrier. The transition kinetic observed in $MAPbBr_3$ is unique and distinguishable from inorganic MHPs in which the metal ions of A-site are isotropic but is ubiquitous in the organic MHPs as the organic cation has the directionality and anisotropic interaction with the octahedra.

4. CONCLUSIONS

In summary, we have demonstrated different transition routes in $MAPbBr_3$ at high $P-T$ conditions, wherein a layered edge-shared octahedral crystalline phase has been revealed via multiple-stage crystallization from the pressure-induced amorphous phase. Upon heating at 8.7 GPa, the amorphized $MAPbBr_3$ crystallizes at 591 K, followed by several crystal−crystal transitions upon further heating to 654 K and finally forms a stable high $P-T$ structure. The structural analysis demonstrated that the high $P-T$ phase possesses a monoclinic

https://doi.org/10.1021/acs.chemmater.2c03172
Chem. Mater. XXXX, XXX, XXX−XXX

$P2/m$ structure, which can be quenched to RT at high pressure but recovered to the original perovskite structure ($Pm\bar{3}m$) below 0.7 GPa under decompression. The Raman and optical measurements indicate that the high $P-T$ phase has characteristic vibrational and tunable optical properties similar to those of the amorphous phase, implying the similarity of the local structure in both MA ligands and $PbBr_6$ octahedra. Therefore, we propose that the amorphization of $MAPbBr_3$ is derived from the random orientation of MA cations during compression and the subsequent anisotropic interaction between MA cations and Br−Pb octahedra. This behavior results in the disordered arrangement of the $PbBr_6$ octahedra and the kinetic barrier for the transformation from the amorphous phase into the high-pressure crystalline phase can be overcome upon heating. On the other hand, the transformation from the initial perovskite structure into the high $P-T$ phase can be realized without amorphization because sufficient thermal energy has been provided in this case. The present results demonstrate the structural diversity and different transformation routes in $MAPbBr_3$, distinguishable from inorganic MHPs with the isotropic metal ion in the A-site but ubiquitous in 3D organic MHPs. Our findings provide new insights into understanding the formation of the amorphization mechanism and, more broadly, the understanding and exploration of the structure−property relationship of MHPs.

■ ASSOCIATED CONTENT

Supporting Information

The Supporting Information is available free of charge at https://pubs.acs.org/doi/10.1021/acs.chemmater.2c03172.

Structural evolution of $MAPbBr_3$ under high pressure; structural evolution from the amorphous $MAPbBr_3$ to the intermediate metastable phase under high $P-T$ conditions; temperature-induced structural evolution of quenched high $P-T$ phase and original $MAPbBr_3$; in situ high-pressure Raman of $MAPbBr_3$ at RT; selected Raman spectra of high $P-T$ phase of $MAPbBr_3$; absorption and band gap of $MAPbBr_3$, high $P-T$ phase, and amorphous phase under high pressure; PL evolution of original $MAPbBr_3$; and PL peak position and intensity of high $P-T$ phase (PDF)

■ AUTHOR INFORMATION

Corresponding Authors

Xujie Lü − *Center for High Pressure Science and Technology Advanced Research (HPSTAR), Beijing 100094, China;* orcid.org/0000-0001-8402-7160; Email: xujie.lu@hpstar.ac.cn

Chuanlong Lin − *Center for High Pressure Science and Technology Advanced Research (HPSTAR), Beijing 100094, China;* orcid.org/0000-0001-7218-816X; Email: chuanlong.lin@hpstar.ac.cn

Authors

Mei Li − *Center for High Pressure Science and Technology Advanced Research (HPSTAR), Beijing 100094, China;* orcid.org/0000-0001-7892-6688

Kejun Bu − *Center for High Pressure Science and Technology Advanced Research (HPSTAR), Beijing 100094, China;* orcid.org/0000-0002-1466-2764

Junlong Li − *Center for High Pressure Science and Technology Advanced Research (HPSTAR), Beijing 100094, China; Beijing Synchrotron Radiation Facility, Institute of High Energy Physics, Chinese Academy of Science, Beijing 100049, China*

Hao Wang − *Center for High Pressure Science and Technology Advanced Research (HPSTAR), Beijing 100094, China*

Yixuan Xu − *Beijing Synchrotron Radiation Facility, Institute of High Energy Physics, Chinese Academy of Science, Beijing 100049, China*

Songhao Guo − *Center for High Pressure Science and Technology Advanced Research (HPSTAR), Beijing 100094, China;* orcid.org/0000-0003-0570-0164

Hui Luo − *Center for High Pressure Science and Technology Advanced Research (HPSTAR), Beijing 100094, China*

Bingyan Liu − *Center for High Pressure Science and Technology Advanced Research (HPSTAR), Beijing 100094, China*

Dongliang Yang − *Beijing Synchrotron Radiation Facility, Institute of High Energy Physics, Chinese Academy of Science, Beijing 100049, China*

Yu Gong − *Beijing Synchrotron Radiation Facility, Institute of High Energy Physics, Chinese Academy of Science, Beijing 100049, China*

Yonggang Wang − *Center for High Pressure Science and Technology Advanced Research (HPSTAR), Beijing 100094, China;* orcid.org/0000-0003-4816-9182

Yufeng Liu − *School of Materials and Engineering, Shanghai Institute of Technology, Shanghai 200235, China;* orcid.org/0000-0002-2733-7733

Complete contact information is available at: https://pubs.acs.org/10.1021/acs.chemmater.2c03172

Notes

The authors declare no competing financial interest.

■ ACKNOWLEDGMENTS

This work was supported by the National Nature Science Foundation of China (NSFC) (grant nos. 11974033, 22275004, and U2141240), Shanghai Science and Technology Committee (no. 22JC1410300), Shanghai Key Laboratory of Novel Extreme Condition Materials (no. 22dz2260800), and the Shanghai Natural Science Foundation (grant no. 20ZR1455400). The XRD measurements were performed at the 4W2 HP-Station, Beijing Synchrotron Radiation Facility (BSRF), which is supported by the Chinese Academy of Sciences (grant nos. KJCX2-SW-N03 and KJCX2-SW-N20).

■ REFERENCES

(1) Zuo, C.; Bolink, H. J.; Han, H.; Huang, J.; Cahen, D.; Ding, L. Advances in Perovskite Solar Cells. *Adv. Sci.* **2016**, *3*, 1500324.

(2) Giustino, F.; Snaith, H. J. Toward Lead-Free Perovskite Solar Cells. *ACS Energy Lett.* **2016**, *1*, 1233−1240.

(3) Worku, M.; Ben-Akacha, A.; Blessed Shonde, T.; Liu, H.; Ma, B. The Past, Present, and Future of Metal Halide Perovskite Light-Emitting Diodes. *Small Sci.* **2021**, *1*, 2000072.

(4) Friend, R. H.; Di, D.; Lilliu, S.; Zhao, B. Perovskite LEDs. *Sci. Video Protoc.* **2019**, *1*, 1−5.

(5) Zhou, Y.; Chen, J.; Bakr, O. M.; Mohammed, O. F. Metal Halide Perovskites for X-Ray Imaging Scintillators and Detectors. *ACS Energy Lett.* **2021**, *6*, 739−768.

(6) Grancini, G.; Marras, S.; Prato, M.; Giannini, C.; Quarti, C.; De Angelis, F.; De Bastiani, M.; Eperon, G. E.; Snaith, H. J.; Manna, L.; Petrozza, A. The Impact of the Crystallization Processes on the

Structural and Optical Properties of Hybrid Perovskite Films for Photovoltaics. *J. Phys. Chem. Lett.* **2014**, *5*, 3836−3842.
(7) Luo, S.; Daoud, W. A. Crystal Structure Formation of $CH_3NH_3PbI_{3-X}Cl_x$ Perovskite. *Materials* **2016**, *9*, 1−13.
(8) Guo, S.; Bu, K.; Li, J.; Hu, Q.; Luo, H.; He, Y.; Wu, Y.; Zhang, D.; Zhao, Y.; Yang, W.; Kanatzidis, M. G.; Lü, X. Enhanced Photocurrent of All-Inorganic Two-Dimensional Perovskite $Cs_2PbI_2Cl_2$ via Pressure-Regulated Excitonic Features. *J. Am. Chem. Soc.* **2021**, *143*, 2545−2551.
(9) Senocrate, A.; Spanopoulos, I.; Zibouche, N.; Maier, J.; Islam, M. S.; Kanatzidis, M. G. Tuning Ionic and Electronic Conductivities in the "Hollow" Perovskite {*en*}$MAPbI_3$. *Chem. Mater.* **2021**, *33*, 719−726.
(10) Spanopoulos, I.; Ke, W.; Stoumpos, C. C.; Schueller, E. C.; Kontsevoi, O. Y.; Seshadri, R.; Kanatzidis, M. G. Unraveling the Chemical Nature of the 3D "Hollow" Hybrid Halide Perovskites. *J. Am. Chem. Soc.* **2018**, *140*, 5728−5742.
(11) Guo, S.; Zhao, Y.; Bu, K.; Fu, Y.; Luo, H.; Chen, M.; Hautzinger, M. P.; Wang, Y.; Jin, S.; Yang, W.; Lü, X. Pressure-Suppressed Carrier Trapping Leads to Enhanced Emission in Two-Dimensional Perovskite $(HA)_2(GA)Pb_2I_7$. *Angew. Chem. Int. Ed.* **2020**, *132*, 17686−17692.
(12) Sun, Q.; Yin, W. J. Thermodynamic Stability Trend of Cubic Perovskites. *J. Am. Chem. Soc.* **2017**, *139*, 14905−14908.
(13) Bai, F.; Bian, K.; Huang, X.; Wang, Z.; Fan, H. Pressure Induced Nanoparticle Phase Behavior, Property, and Applications. *Chem. Rev.* **2019**, *119*, 7673−7717.
(14) Li, H.; Qin, Y.; Shan, B.; Shen, Y.; Ersan, F.; Soignard, E.; Ataca, C.; Tongay, S. Unusual Pressure-Driven Phase Transformation and Band Renormalization in 2D VdW Hybrid Lead Halide Perovskites. *Adv. Mater.* **2020**, *32*, 1−7.
(15) Postorino, P.; Malavasi, L. Pressure-Induced Effects in Organic-Inorganic Hybrid Perovskites. *J. Phys. Chem. Lett.* **2017**, *8*, 2613−2622.
(16) Liu, S.; Sun, S.; Gan, C. K.; Del Águila, A. G.; Fang, Y.; Xing, J.; Thu Ha Do, T.; White, T. J.; Li, H.; Huang, W.; Xiong, Q. Manipulating Efficient Light Emission in Two-Dimensional Perovskite Crystals by Pressure-Induced Anisotropic Deformation. *Sci. Adv.* **2019**, *5*, 1−11.
(17) Luo, H.; Guo, S.; Zhang, Y.; Bu, K.; Lin, H.; Wang, Y.; Yin, Y.; Zhang, D.; Jin, S.; Zhang, W.; Yang, W.; Ma, B.; Xujie, L. Regulating Exciton−Phonon Coupling to Achieve a Near-Unity Photoluminescence Quantum Yield in One-Dimensional Hybrid Metal Halides. *Adv. Sci.* **2021**, *8*, 2100786.
(18) Jaffe, A.; Lin, Y.; Beavers, C. M.; Voss, J.; Mao, W. L.; Karunadasa, H. I. High-Pressure Single-Crystal Structures of 3D Lead-Halide Hybrid Perovskites and Pressure Effects on Their Electronic and Optical Properties. *ACS Cent. Sci.* **2016**, *2*, 201−209.
(19) Lü, X.; Stoumpos, C.; Hu, Q.; Ma, X.; Zhang, D.; Guo, S.; Hoffman, J.; Bu, K.; Guo, X.; Wang, Y.; Ji, C.; Chen, H.; Xu, H.; Jia, Q.; Yang, W.; Kanatzidis, M. G.; Mao, H. K. Regulating Off-Centering Distortion Maximizes Photoluminescence in Halide Perovskites. *Natl. Sci. Rev.* **2021**, *8*, nwaa288.
(20) Bu, K.; Hu, Q.; Qi, X.; Wang, D.; Guo, S.; Luo, H.; Lin, T.; Guo, X.; Zeng, Q.; Ding, Y.; Huang, F.; Yang, W.; Mao, H. K.; Lü, X. Nested Order-Disorder Framework Containing a Crystalline Matrix with Self-Filled Amorphous-like Innards. *Nat. Commun.* **2022**, *13*, 4650.
(21) Chen, M.; Guo, S.; Bu, K.; Lee, S.; Luo, H.; Wang, Y.; Liu, B.; Yan, Z.; Dong, H.; Yang, W.; Ma, B.; Lü, X. Pressure-Induced Robust Emission in a Zero-Dimensional Hybrid Metal Halide $(C_9NH_{20})_6Pb_3Br_{12}$. *Matter Radiat. Extremes* **2021**, *6*, 058401.
(22) Ke, F.; Wang, C.; Jia, C.; Wolf, N. R.; Yan, J.; Niu, S.; Devereaux, T. P.; Karunadasa, H. I.; Mao, W. L.; Lin, Y. Preserving a Robust $CsPbI_3$ Perovskite Phase via Pressure-Directed Octahedral Tilt. *Nat. Commun.* **2021**, *12*, 461.
(23) Noculak, A.; Boehme, S. C.; Aebli, M.; Shynkarenko, Y.; McCall, K. M.; Kovalenko, M. V. Pressure-Induced Perovskite-to-Non-Perovskite Phase Transition in $CsPbBr_3$. *Helv. Chim. Acta* **2021**, *104*, No. e2000222.
(24) Li, M.; Peng, S.; Fang, S.; Gong, Y.; Yang, D.; Bu, K.; Liu, B.; Luo, H.; Guo, S.; Li, J.; Wang, H.; Liu, Y.; Jiang, S.; Lin, C.; Lü, X. Synthesis of Two-Dimensional $CsPb_2X_5$ (X = Br and I) with a Stable Structure and Tunable Bandgap by $CsPbX_3$ Phase Separation. *J. Phys. Chem. Lett.* **2022**, *13*, 2555−2562.
(25) Wang, Y.; Lü, X.; Yang, W.; Wen, T.; Yang, L.; Ren, X.; Wang, L.; Lin, Z.; Zhao, Y. Pressure-Induced Phase Transformation, Reversible Amorphization, and Anomalous Visible Light Response in Organolead Bromide Perovskite. *J. Am. Chem. Soc.* **2015**, *137*, 11144−11149.
(26) Swainson, I. P.; Tucker, M. G.; Wilson, D. J.; Winkler, B.; Milman, V. Pressure Response of an Organic-Inorganic Perovskite: Methylammonium Lead Bromide. *Chem. Mater.* **2007**, *19*, 2401−2405.
(27) Kong, L.; Liua, G.; Gong, J.; Hu, Q.; Schaller, R. D.; Dera, P.; Zhang, D.; Liu, Z.; Yang, W.; Zhu, K.; Tang, Y.; Wang, C.; Wei, S. H.; Xu, T.; Mao, H. K. Simultaneous Band-Gap Narrowing and Carrier-Lifetime Prolongation of Organic-Inorganic Trihalide Perovskites. *Proc. Natl. Acad. Sci. U.S.A.* **2016**, *113*, 8910−8915.
(28) Tan, M.; Wang, S.; Rao, F.; Yang, S.; Wang, F. Pressures Tuning the Band Gap of Organic−Inorganic Trihalide Perovskites ($MAPbBr_3$): A First-Principles Study. *J. Electron. Mater.* **2018**, *47*, 7204−7211.
(29) Huang, Y.; Wang, L.; Ma, Z.; Wang, F. Pressure-Induced Band Structure Evolution of Halide Perovskites: A First-Principles Atomic and Electronic Structure Study. *J. Phys. Chem. C* **2019**, *123*, 739−745.
(30) Capitani, F.; Marini, C.; Caramazza, S.; Dore, P.; Pisanu, A.; Malavasi, L.; Nataf, L.; Baudelet, F.; Brubach, J. B.; Roy, P.; Postorino, P. Locking of Methylammonium by Pressure-Enhanced H-Bonding in $(CH_3NH_3)PbBr_3$ Hybrid Perovskite. *J. Phys. Chem. C* **2017**, *121*, 28125−28131.
(31) Shi, D.; Adinolfi, V.; Comin, R.; Yuan, M.; Alarousu, E.; Buin, A.; Chen, Y.; Hoogland, S.; Rothenberger, A.; Katsiev, K.; Losovyj, Y.; Zhang, X.; Dowben, P. A.; Mohammed, O. F.; Sargent, E. H.; Bakr, O. M. Low Trap-State Density and Long Carrier Diffusion in Organolead Trihalide Perovskite Single Crystals. *Science* **2015**, *347*, 519−522.
(32) Wang, K. H.; Li, L. C.; Shellaiah, M.; Sun, K. W. Structural and Photophysical Properties of Methylammonium Lead Tribromide ($MAPbBr_3$) Single Crystals. *Sci. Rep.* **2017**, *7*, 13643.
(33) Mao, H. K.; Bell, P. M.; Shaner, J. W.; Steinberg, D. J. Specific Volume Measurements of Cu, Mo, Pd, and Ag and Calibration of the Ruby R1 Fluorescence Pressure Gauge from 0.06 to 1 Mbar. *J. Appl. Phys.* **1978**, *49*, 3276−3283.
(34) Prescher, C.; Prakapenka, V. B. DIOPTAS: A Program for Reduction of Two-Dimensional X-Ray Diffraction Data and Data Exploration. *High Press. Res.* **2015**, *35*, 223−230.
(35) Toby, B. H. EXPGUI, a Graphical User Interface for GSAS. *J. Appl. Crystallogr.* **2001**, *34*, 210−213.
(36) Lin, C.; Smith, J. S.; Sinogeikin, S. V.; Kono, Y.; Park, C.; Kenney-Benson, C.; Shen, G. A Metastable Liquid Melted from a Crystalline Solid under Decompression. *Nat. Commun.* **2017**, *8*, 14260.
(37) Lin, C.; Smith, J. S.; Liu, X.; Tse, J. S.; Yang, W. Venture into Water's No Man's Land: Structural Transformations of Solid H_2O under Rapid Compression and Decompression. *Phys. Rev. Lett.* **2018**, *121*, 225703.
(38) Lin, C.; Liu, X.; Yong, X.; Tse, J. S.; Smith, J. S.; English, N. J.; Wang, B.; Li, M.; Yang, W.; Mao, H. K. Temperature-Dependent Kinetic Pathways Featuring Distinctive Thermal-Activation Mechanisms in Structural Evolution of Ice VII. *Proc. Natl. Acad. Sci. U.S.A.* **2020**, *117*, 15437−15442.
(39) Lin, C.; Liu, X.; Yang, D.; Li, X.; Smith, J. S.; Wang, B.; Dong, H.; Li, S.; Yang, W.; Tse, J. S. Temperature- and Rate-Dependent Pathways in Formation of Metastable Silicon Phases under Rapid Decompression. *Phys. Rev. Lett.* **2020**, *125*, 155702.

https://doi.org/10.1021/acs.chemmater.2c03172
Chem. Mater. XXXX, XXX, XXX−XXX

(40) Onoda-Yamamuro, N.; Yamamuro, O.; Matuso, T.; Suga, H. P.-T. Phase Relations of $CH_3NH_3PbX_3$ (X = Cl, Br, I) Crystals. *J. Phys. Chem. Solids* **1992**, *53*, 277−281.
(41) Shirako, Y.; Kojitani, H.; Oganov, A. R.; Fujino, K.; Miura, H.; Mori, D.; Inaguma, Y.; Yamaura, K.; Akaogi, M. Crystal Structure of $CaRhO_3$ Polymorph: High-Pressure Intermediate Phase between Perovskite and Post-Perovskite. *Am. Mineral.* **2012**, *97*, 159−163.
(42) Mao, L.; Guo, P.; Kepenekian, M.; Hadar, I.; Katan, C.; Even, J.; Schaller, R. D.; Stoumpos, C. C.; Kanatzidis, M. G. Structural Diversity in White-Light-Emitting Hybrid Lead Bromide Perovskites. *J. Am. Chem. Soc.* **2018**, *140*, 13078−13088.
(43) Mao, L.; Stoumpos, C. C.; Kanatzidis, M. G. Two-Dimensional Hybrid Halide Perovskites: Principles and Promises. *J. Am. Chem. Soc.* **2019**, *141*, 1171−1190.
(44) Onoda-Yamamuro, N.; Matsuo, T.; Suga, H. Calorimetric and IR Spectroscopic Studies of Phase Transitions in Methylammonium Trihalogenoplumbates (II). *J. Phys. Chem. Solids* **1990**, *51*, 1383−1395.
(45) Niemann, R. G.; Kontos, A. G.; Palles, D.; Kamitsos, E. I.; Kaltzoglou, A.; Brivio, F.; Falaras, P.; Cameron, P. J. Halogen Effects on Ordering and Bonding of $CH_3NH_3^+$ in $CH_3NH_3PbX_3$ (X = Cl, Br, I) Hybrid Perovskites: A Vibrational Spectroscopic Study. *J. Phys. Chem. C* **2016**, *120*, 2509−2519.
(46) Matsuishi, K.; Ishihara, T.; Onari, S.; Chang, Y. H.; Park, C. H. Optical Properties and Structural Phase Transitions of Lead-Halide Based Inorganic-Organic 3D and 2D Perovskite Semiconductors under High Pressure. *Phys. Status Solidi Basic Res.* **2004**, *241*, 3328−3333.
(47) Wang, L.; Ou, T.; Wang, K.; Xiao, G.; Gao, C.; Zou, B. Pressure-Induced Structural Evolution, Optical and Electronic Transitions of Nontoxic Organometal Halide Perovskite-Based Methylammonium Tin Chloride. *Appl. Phys. Lett.* **2017**, *111*, 233901.
(48) Wang, L.; Wang, K.; Xiao, G.; Zeng, Q.; Zou, B. Pressure-Induced Structural Evolution and Band Gap Shifts of Organometal Halide Perovskite-Based Methylammonium Lead Chloride. *J. Phys. Chem. Lett.* **2016**, *7*, 5273−5279.
(49) Wang, P.; Guan, J.; Galeschuk, D. T. K.; Yao, Y.; He, C. F.; Jiang, S.; Zhang, S.; Liu, Y.; Jin, M.; Jin, C.; Song, Y. Pressure-Induced Polymorphic, Optical, and Electronic Transitions of Formamidinium Lead Iodide Perovskite. *J. Phys. Chem. Lett.* **2017**, *8*, 2119−2125.
(50) Jiang, S.; Fang, Y.; Li, R.; Xiao, H.; Crowley, J.; Wang, C.; White, T. J.; Goddard, W. A.; Wang, Z.; Baikie, T.; Fang, J. Pressure-Dependent Polymorphism and Band-Gap Tuning of Methylammonium Lead Iodide Perovskite. *Angew. Chem., Int. Ed.* **2016**, *55*, 6540−6544.
(51) Wang, L.; Wang, K.; Zou, B. Pressure-Induced Structural and Optical Properties of Organometal Halide Perovskite-Based Formamidinium Lead Bromide. *J. Phys. Chem. Lett.* **2016**, *7*, 2556−2562.
(52) Aebli, M.; Benin, B. M.; McCall, K. M.; Morad, V.; Thöny, D.; Grützmacher, H.; Kovalenko, M. V. White $CsPbBr_3$: Characterizing the One-Dimensional Cesium Lead Bromide Polymorph. *Helv. Chim. Acta* **2020**, *103*, No. e2000080.
(53) Cao, Y.; Qi, G.; Liu, C.; Wang, L.; Ma, Z.; Wang, K.; Du, F.; Xiao, G.; Zou, B. Pressure-Tailored Band Gap Engineering and Structure Evolution of Cubic Cesium Lead Iodide Perovskite Nanocrystals. *J. Phys. Chem. C* **2018**, *122*, 9332−9338.
(54) Liang, Y.; Huang, X.; Huang, Y.; Wang, X.; Li, F.; Wang, Y.; Tian, F.; Liu, B.; Shen, Z. X.; Cui, T. New Metallic Ordered Phase of Perovskite $CsPbI_3$ under Pressure. *Adv. Sci.* **2019**, *6*, 1900399.
(55) Weller, M. T.; Weber, O. J.; Henry, P. F.; Di Pumpo, A. M.; Hansen, T. C. Complete Structure and Cation Orientation in the Perovskite Photovoltaic Methylammonium Lead Iodide between 100 and 352 K. *Chem. Commun.* **2015**, *51*, 4180−4183.
(56) Maalej, A.; Abid, Y.; Kallel, A.; Daoud, A.; Lautié, A.; Romain, F. Phase Transitions and Crystal Dynamics in the Cubic Perovskite $CH_3NH_3PbCl_3$. *Solid State Commun.* **1997**, *103*, 279−284.
(57) Dar, M. I.; Jacopin, G.; Meloni, S.; Mattoni, A.; Arora, N.; Boziki, A.; Zakeeruddin, S. M.; Rothlisberger, U.; Grätzel, M. Origin of Unusual Bandgap Shift and Dual Emission in Organic-Inorganic Lead Halide Perovskites. *Sci. Adv.* **2016**, *2*, No. e1601156.
(58) Ghosh, D.; Walsh Atkins, P.; Islam, M. S.; Walker, A. B.; Eames, C. Good Vibrations: Locking of Octahedral Tilting in Mixed-Cation Iodide Perovskites for Solar Cells. *ACS Energy Lett.* **2017**, *2*, 2424−2429.
(59) Zhang, L.; Wang, L.; Wang, K.; Zou, B. Pressure-Induced Structural Evolution and Optical Properties of Metal-Halide Perovskite $CsPbCl_3$. *J. Phys. Chem. C* **2018**, *122*, 15220−15225.
(60) Szafrański, M.; Katrusiak, A. Mechanism of Pressure-Induced Phase Transitions, Amorphization, and Absorption-Edge Shift in Photovoltaic Methylammonium Lead Iodide. *J. Phys. Chem. Lett.* **2016**, *7*, 3458−3466.
(61) Wang, Z.; Schliehe, C.; Wang, T.; Nagaoka, Y.; Cao, Y. C.; Bassett, W. A.; Wu, H.; Fan, H.; Weller, H. Deviatoric Stress Driven Formation of Large Single-Crystal PbS Nanosheet from Nanoparticles and in Situ Monitoring of Oriented Attachment. *J. Am. Chem. Soc.* **2011**, *133*, 14484−14487.
(62) Zhang, H.; Tóth, O.; Liu, X. D.; Bini, R.; Gregoryanz, E.; Dalladay-Simpson, P.; de Panfilis, S.; Santoro, M.; Gorelli, F. A.; Martoňák, R. Pressure-Induced Amorphization and Existence of Molecular and Polymeric Amorphous Forms in Dense SO_2. *Proc. Natl. Acad. Sci. U.S.A.* **2020**, *117*, 8736−8742.

https://doi.org/10.1021/acs.chemmater.2c03172
Chem. Mater. XXXX, XXX, XXX−XXX